# POLITECNICO DI TORINO
## Repository ISTITUZIONALE

Experimental Assessment of Induction Motors Fed by Sub-MHz-PWM Wide Band Gap Inverters

(Article begins on next page)

02 September 2025

# Experimental Assessment of Induction Motors Fed by Sub-MHz-PWM Wide Band Gap Inverters

Giacomo Scelba, *Senior Member, IEEE*, Daniele Cremente, Giulio De Donato, *Senior Member, IEEE*
Silvio Vaschetto, *Senior Member, IEEE*, Emmanuel Agamloh, *Senior Member, IEEE*, and Andrea Cavagnino, *Fellow, IEEE*

*Abstract*— Three phase inverters with switching frequencies above 100 kHz have recently become feasible thanks to the significant progress made in wide band gap semiconductor technology. The main drivers behind the intense research and development of these ultra-high switching frequency PWM inverters are the extraordinary gravimetric and volumetric power densities that can be achieved. On the other hand, not as much attention has been devoted to the loads that these inverters supply, quite frequently consisting in ac motors. The impact of sub-MHz PWM and of the associated tens of nanoseconds range switching transients on motor terminal overvoltage, common mode currents and losses are still to be discussed exhaustively. The authors have thus decided to investigate what happens to induction motors supplied by inverters having switching frequencies up to 350 kHz. After an introduction on wide band gap semiconductor devices, the paper presents some interesting experimental observations conducted on a 1.1 kW 4-pole induction motor fed by a silicon carbide inverter. Further insight is provided by tests on a laminated steel toroid, supplied by a single-phase full bridge silicon carbide inverter. Discussions on the experimental results highlight the previously unreported impact of common mode losses, which become a predominant part of the PWM harmonic losses.

*Keywords—Induction motors, PWM inverters, wide-bandgap semiconductors, silicon carbide, gallium nitride, automotive applications, parasitic switching effects, common-mode issues.*

## I. INTRODUCTION

The need for power electronic converters having greater compactness and higher performance is behind the push to increase the switching frequency in many energy conversion applications, and is one of the key drivers behind the recent market expansion of wide band gap (WBG) power electronic devices. This concept is widely accepted in several industries, ranging from renewable energy to automotive. In the latter, for example, high speed and low torque ripple electromechanical energy conversion is achieved by means of low-inductance motors supplied by power converters having high switching frequencies and high-bandwidth current control, [1].

WBG power devices, such as silicon carbide (SiC) power MOSFETs and gallium nitride (GaN) FETs are becoming the go-to devices for high-power and high-efficiency electromechanical energy conversion, with switching frequencies in excess of 300 kHz for hard-switched inverters, [2]. Fig.1 shows that the market evolution for SiC and GaN devices is impressive, ensuring very good compound annual growth rates in a short period, [3]-[5]. Therefore, it is expected that WBG inverters will be increasingly used to supply electrical machines, making it interesting and timely to investigate the side effects that come together with ultra-high switching frequencies. The negative effects of hard switching on cables and motors, and possible ways to mitigate them are well documented in the literature. Readers can refer to [6]-[15], just to cite some of the most recent papers concerning the typical phenomena under PWM supply, such as overvoltage at the motor terminals, bearing currents, insulation ageing, partial discharges, electromagnetic interference, iron losses and so on. However, to the best of the authors' knowledge, most of these findings are limited to switching frequencies up to about 50 kHz, also in the few cases where WBG inverters have been used. Very few papers investigate the impact of PWM frequencies up to 200 kHz on iron losses in electric steels, [16].

This paper reports experimental observations of the above phenomena in PWM-fed induction motors (IMs) when the switching frequency well exceeds 100 kHz. Consequently, its main goal is to disseminate data and findings on the effects of high switching frequencies on a standard mains-supply-designed IM fed by a SiC inverter. The authors present the test rig, the measurement challenges, and the no-load and locked-rotor test campaigns. Load tests are not performed due to the absence of a suitable test bench. Nonetheless, this isn't considered a significant limitation since that the impact of inverter supply is substantially independent from the load conditions, as recognized by international standards for efficiency labelling.
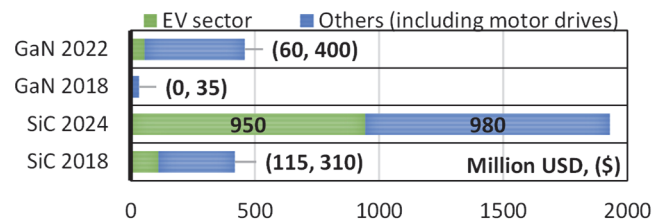
Fig. 1: Market evolution for the SiC and GaN devices (adapted from [3], [4]).
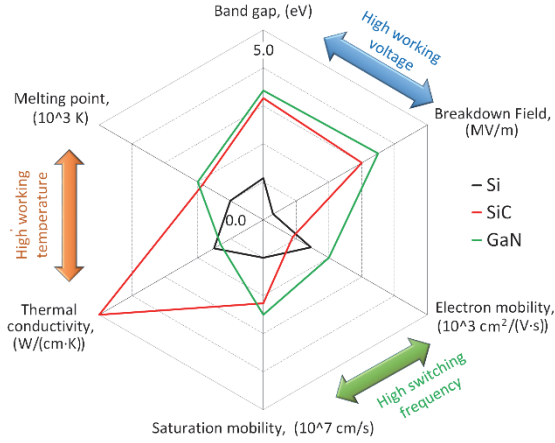
Fig. 2: Comparison of the main proprierties of silicon, silicon carbide, and gallium nitride.
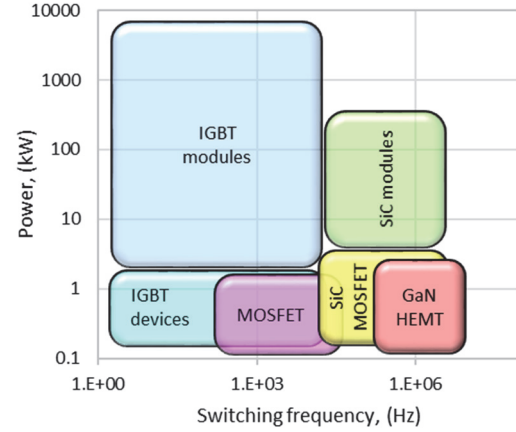


Fig. 3: Typical categorization of power electronic devices in the power-switching frequency plane, (adapted from [5]).

Different cable lengths and switching frequencies (up to 350 kHz) have been investigated. This paper is an extension of [17], reporting previously unpublished iron loss measurements on a toroidal core made from the same electrical steel of the IM and a discussion providing insight into motor losses and highlighting the significant impact of common mode losses, which become a predominant part of the PWM harmonic losses.

## II. SiC AND GaN TECHNOLOGY OVERVIEW

Significant developments in WBG semiconductor technology have allowed to obtain power electronic devices with significantly higher efficiency and power density compared to their silicon-based counterparts. The reason lies in the physical properties of SiC and GaN, as illustrated in Fig. 2, which allow higher breakdown voltages, switching frequencies and operating temperatures, with lower losses. Fig. 3 shows how Si, SiC and Gan devices compare in the power vs switching frequency plane. WBG devices are perfectly suited to high-speed drives, which require inverters able to supply high fundamental frequency output voltages. Furthermore, they are also an ideal match for aerospace and automotive applications, where the maximization of power density and efficiency is crucial.

Presently, SiC technology is more mature than GaN technology. In the market, it is possible to find – in addition to discrete components and half-bridge modules – several dc/ac and dc/dc SiC-based converters; Fig. 4 shows some examples.

GaN devices are available almost only discrete form; a few half-bridge modules have been introduced in the market over the past year. In automotive applications it seems that both technologies can already coexist: SiC-based converters can ensure the right power level to drive the traction motor, while GaN devices may be used for on-board battery charging. It should be mentioned that it is a common practice to deliberately limit the switching frequency and the dv/dt in SiC-based inverters to values comparable to those used in Si IGBTs. This is done to limit electromagnetic interference (EMI) and voltage stress on the motor windings. Nonetheless, SiC devices are still preferred over Si due to their significantly lower switching losses.

The four discrete devices listed in Table I are examples of state of the art, automotive grade Si, SiC and GaN devices for hard switching applications. The SiC power MOSFET and GaN FET are rated for a maximum drain to source voltage of 900 V, while the other devices are rated for 650 V. It should be mentioned that while both power MOSFETs and the 650 V GaN HEMT are inherently normally-off devices, the 900 V GaN FET is a combination of a normally-on GaN HEMT and a low voltage Si power MOSFET, known as a Baliga-Pair, [2].

In terms of current handling, the maximum continuous drain currents indicated on the datasheets are frequently given for a 25°C case temperature, so a non-negligible derating is required if the case heats up. Table I shows that the maximum current drops by over 35% for the MOSFET and the GaN FET and by 22% for the GaN HEMT if the case is at 100°C.
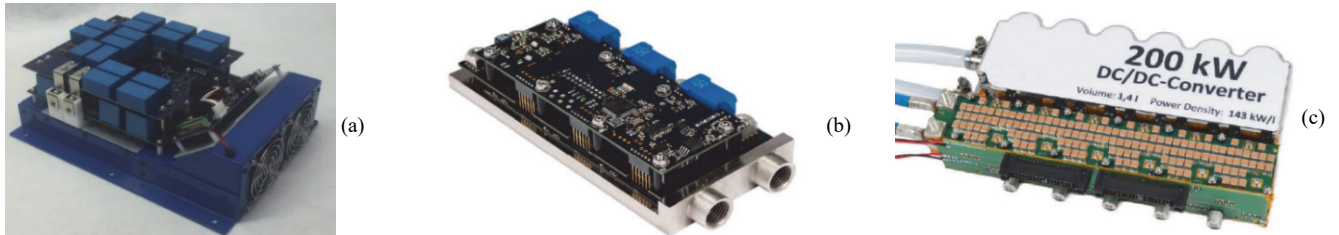


Fig. 4: Examples of SiC based converters: (a) air cooled 30kW general purpose inverter, 3.5 kW/l; (b) 60 kW inverter for high-speed drives, 160 kW/l; (c) bidirectional 200 kW dc/dc converter for automotive, 143 kW/l.

TABLE I
COMPARISON OF COMMERCIALLY AVAILABLE SI, SIC AND GAN DEVICES

| Device Technology | Si MOSFET | SiC MOSFET | GaN HEMT | GaN FET (Baliga-Pair) |
|---|---|---|---|---|
| Maximum drain-to-source voltage | 650 V | 1200 V | 650 V | 900 V |
| Maximum continuous current for $T_c$ = 25 °C | 60 A | 66 A | 60 A | 34 A |
| Maximum continuous current for $T_c$ = 100 °C | 38 A | 48 A | 47 A | 22 A |
| Static $R_{ds(on)}$ at max. cont. current for $T_j$ = 150 °C | 100 mΩ | 40 mΩ | 25 mΩ | 63 mΩ |
| Turn on time | 50 ns (@ $V_{DD}$ = 400 V) | 75 ns (@ $V_{DD}$ = 800 V) | 17 ns (@ $V_{DD}$ = 400 V) | 73 ns (@ $V_{DD}$ = 600 V) |
| Turn off time | 110 ns (@ $V_{DD}$ = 400 V) | 37 ns (@ $V_{DD}$ = 800 V) | 36 ns (@ $V_{DD}$ = 400 V) | 70 ns (@ $V_{DD}$ = 600 V) |
| Maximum dv/dt | 50 V/ns | 50 V/ns | 100 V/ns | 100 V/ns |
| Reverse recovery charge | 17 μC | 624 nC | 0 nC | 165 nC |
| Cost (over 1,000-2,000 components) | 15 € | 17 € | 35 € | 14 € |

In terms of switching speeds, Table I shows that the Si MOSFET is outperformed by the SiC and GaN devices, with the GaN HEMT being the fastest. Another important element to consider when comparing the devices is the reverse recovery charge, which has an impact on the freewheeling capability of the devices and on EMI emissions.

The SiC power MOSFET has a significantly reduced amount of reverse recovery charge compared to the Si counterpart. On the other hand, GaN HEMTs have inherently zero reverse recovery charge due to their lateral structure, without any body diode. The GaN Baliga-Pair has a small amount of reverse recovery charge due to the presence of the body diode in the low voltage MOSFET. Regardless of the technology, no datasheet gives information on the maximum switching frequencies for hard switching, since these are highly dependent on the converter and cooling system designs.

## III. IMPACT OF PWM ON CABLE - MOTOR LOADS

At an industrial level, discrete IGBT devices and three-phase modules have been the default solutions for standard variable frequency drives (VFDs) over the past three decades. Furthermore, today's sales data indicates that market penetration of IGBT technology is by no means in decline. Fig. 3 clearly shows the importance of this technology in covering the highest power levels, with switching frequencies up to about 50 kHz.

The impact of PWM on the cable-motor system has been extensively investigated in the literature and all the related issues are understood and have been substantially mitigated. Among them, it is worth to mention overvoltage at the motor terminals, common mode currents, additional losses with consequent reduction in motor efficiency.

It is the authors' opinion that these aspects haven't yet been adequately investigated for switching frequency well above 100 kHz: do similar or additional effects exist and with what severity? It is also to be expected that conducted and radiated electromagnetic interference will increase, producing undesirable effects on nearby electronic devices; nonetheless this isn't the focus of this paper, which is devoted to the inverter-cable-IM system alone. At this point, it is worthwhile summarizing two key phenomena observed in industrial motor-drives.

### A. Overvoltage at Motor Terminals

VFDs supply motors with PWM voltages having short rise and fall times. These pulses propagate along the cable and, in combination with the mismatch between the cable and machine impedances, are subjected to reflection which causes overvoltage to appear at the motor terminals [11]. Such an undesired effect is more evident when sufficiently long power-supply cables are used to connect the inverter to the motor, causing overvoltage up to twice the *dc* bus voltage, [12]. In fact, according to wave propagation theory, it is possible to define a critical length $l_c$, corresponding to the cable length at which the overshoot factor $k_V$ is equal to two for a single pulse. This is a function of the rise time $t_r$, the cable parameters, and the propagation speed *c*, [17]:

$$l_c = c\frac{t_r}{2} \quad \text{where} \quad c = \frac{1}{\sqrt{L_0 C_0}} \qquad (1)$$

Additionally, overvoltage up to four times the *dc* bus voltage can be generated by the double pulse phenomenon, [11]. This is a significant cause of winding insulation degradation.

### B. Common Mode Currents

PWM also causes the circulation of common mode currents, which represent a frequent reason for motor and drive failures. In fact, common mode voltages due to PWM usually contain transitions between different voltage levels, the rapidity of which depends on the device technology, [18]. Since motors are usually grounded at the stator frame, the fluctuation of the common-mode voltage generates currents that flow to the ground through parasitic capacitances between the stator windings and the motor frame. The amplitude of such currents depends on the rate of variation of the common-mode voltage and increases with switching frequency, [18].

## IV. EXPERIMENTAL SETUP

Laboratory tests have been performed on a test rig consisting of a three-phase voltage source inverter built with discrete 650V SiC devices, i.e. SCTW100N65G2AG, driven by galvanically isolated single channel MOSFET drivers, i.e. 1EDI60N12AF. The SiC inverter has been designed and assembled in-house and is visible in Fig. 5. The gate signals are generated by a dSpace 1104 controller board and are transmitted to the inverter via fiber-optic cables.
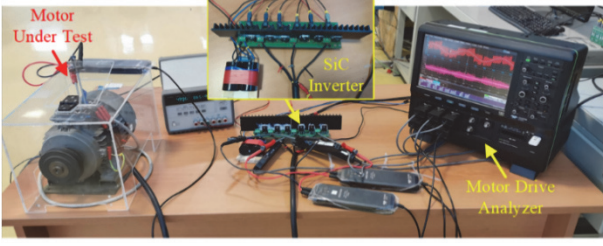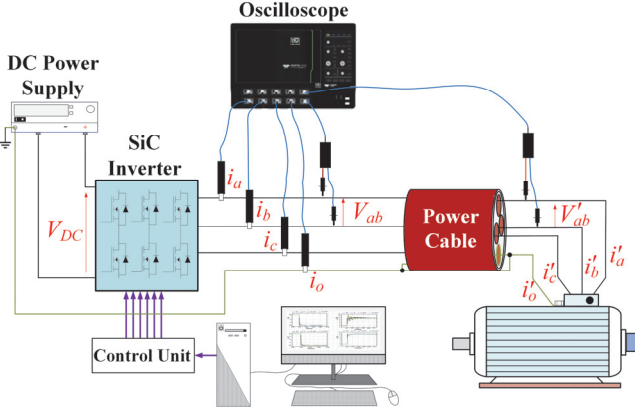
Fig. 5: Measurement test rig setup.



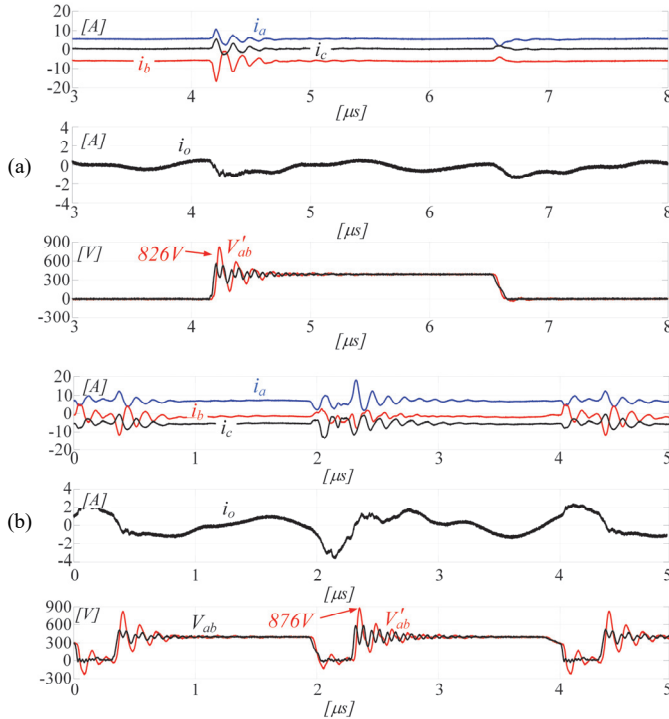Fig. 6: The layout of the measurement system.



Fig. 7: Example of measured waveforms at 25 kHz and 250 kHz switching frequencies (3 m long cable, 150 ns deadtime, 25 ns risetime).

In order to perform no load and blocked rotor tests, open loop independent voltage and frequency regulation has been implemented in the control board. The nameplate of the IM is shown in Table II.
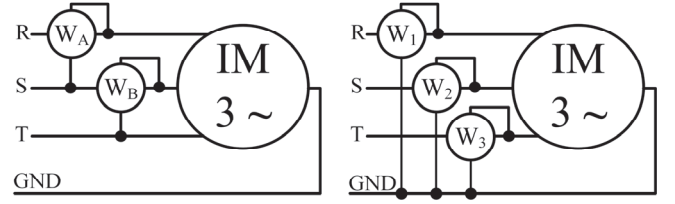


Fig. 8: Aron connection (left) and 4-wire connection (right) for active power measurements.

TABLE II
NAMEPLATE DATA OF THE TESTED MOTOR

| Power, (W) | 1100 |
|---|---|
| Speed, (rpm) | 1400 |
| Voltage, (V) | 230 |
| Current, (A) | 5.2 |
| Frequency, (Hz) | 50 |
| Pole pairs | 2 |
| Connection | Delta |

A sine-triangle PWM technique is employed to drive the inverter. No filters are connected at the inverter output, and variable length shielded three-phase cables (Lapp ölflex classic 110 CY black 0.6/1 kV, 4 conductors; insulation, inner sheath and outer sheath in PVC) have been used to connect the inverter to the motor. The shield is grounded at both ends. A dc power supply is used to provide a *dc* bus voltage equal to 400 V. The dc-link capacitors have a total capacitance of 800 µF. Phase current and voltage waveforms are acquired by an 8 channel, 12-bit resolution oscilloscope (LeCroy MDA810A). Power, overvoltage and common-mode current measurements have been performed using three 30 A, 50 MHz Current Probes (LeCroy CP030) and three 1 kV, 120 MHz High Voltage differential probes (LeCroy HVD3106); the sample rate of the scope is set to 10 MS/s. The common mode current is obtained by summing the measured line currents. A detailed layout of the setup is shown in Fig. 6.

To compensate for the unavoidable fluctuations of the readings under inverter supply, which affects the measured active power, multiple 200 ms window measurements are taken to average out the readings. Fig. 7 shows an example of the line-to-line voltages measured at the inverter output terminals and at the motor terminals, for a 3m long cable and for two different switching frequencies. The measured motor phase currents $i_a$, $i_b$, $i_c$ and the common mode current $i_0$ are also displayed in the same figure.

The oscilloscope is qualified to measure both the fundamental harmonic and rms values of the electrical quantities, as well as the active power; the last quantity is necessary for the no-load and blocked-rotor tests. Considering the bandwidths of the voltage and current probes and the chosen sample rate of the oscilloscope, the authors are quite confident that harmonic components up to about 3 MHz are measured with very limited phase shifts. To further confirm this, the authors preliminarily compared the active power calculated by averaging the instantaneous power to that obtained via the summation of the individual harmonic contributions; an excellent agreement was found between the two approaches.

| Switching frequency, (kHz) | 25 | 100 | 200 | 250 | 300 | 350 | 'average' |
|---|---|---|---|---|---|---|---|
| Cable length = 0.3 m | | | | | | | |
| Inverter output voltage, ($V_{peak}$) | 627 | 613 | 624 | 644 | 675 | 647 | 638 |
| Motor input voltage, ($V_{peak}$) | 740 | 732 | 765 | 767 | 817 | 800 | 770 |
| Common mode current @ inverter output, ($A_{peak-to-peak}$) | 3.42 | 4.08 | 3.94 | 3.72 | 4.00 | 4.06 | 3.87 |
| Common mode current @ inverter output, ($A_{rms}$) | 0.22 | 0.33 | 0.35 | 0.37 | 0.39 | 0.43 | 0.35 |
| Common mode current @ motor input, ($A_{rms}$) | n.a. | n.a. | n.a. | n.a. | n.a. | n.a. | n.a. |
| Cable length = 3.0 m | | | | | | | |
| Inverter output voltage, ($V_{peak}$) | 575 | 571 | 579 | 603 | 591 | 598 | 586 |
| Motor input voltage, ($V_{peak}$) | 844 | 863 | 860 | 853 | 868 | 869 | 859 |
| Common mode current @ inverter output, ($A_{peak-to-peak}$) | 4.36 | 4.92 | 5.38 | 4.24 | 4.12 | 4.60 | 4.60 |
| Common mode current @ inverter output, ($A_{rms}$) | 0.29 | 0.44 | 0.54 | 0.49 | 0.49 | 0.53 | 0.46 |
| Common mode current @ motor input, ($A_{rms}$) | 0.19 | 0.34 | 0.40 | 0.39 | 0.39 | 0.44 | 0.36 |
| Cable length = 10 m | | | | | | | |
| Inverter output voltage, ($V_{peak}$) | 584 | 576 | 596 | 632 | 584 | 584 | 594 |
| Motor input voltage, ($V_{peak}$) | 876 | 915 | 935 | 958 | 938 | 876 | 924 |
| Common mode current @ inverter output, ($A_{peak-to-peak}$) | 6.48 | 7.34 | 5.82 | 6.60 | 4.92 | 6.48 | 6.23 |
| Common mode current @ inverter output, ($A_{rms}$) | 0.45 | 0.82 | 0.78 | 1.06 | 0.53 | 0.45 | 0.73 |
| Common mode current @ motor input, ($A_{rms}$) | 0.15 | 0.29 | 0.26 | 0.35 | 0.22 | 0.15 | 0.25 |
| Cable length = 30 m | | | | | | | |
| Inverter output voltage, ($V_{peak}$) | 581 | 601 | n.a. | n.a. | n.a. | n.a. | 591 |
| Motor input voltage, ($V_{peak}$) | 1031 | 1188 | n.a. | n.a. | n.a. | n.a. | 1110 |
| Common mode current @ inverter output, ($A_{peak-to-peak}$) | 12.70 | 9.42 | n.a. | n.a. | n.a. | n.a. | 11.1 |
| Common mode current @ inverter output, ($A_{rms}$) | 0.99 | 1.63 | n.a. | n.a. | n.a. | n.a. | 1.31 |
| Common mode current @ motor input, ($A_{rms}$) | 0.14 | 0.27 | n.a. | n.a. | n.a. | n.a. | 0.21 |
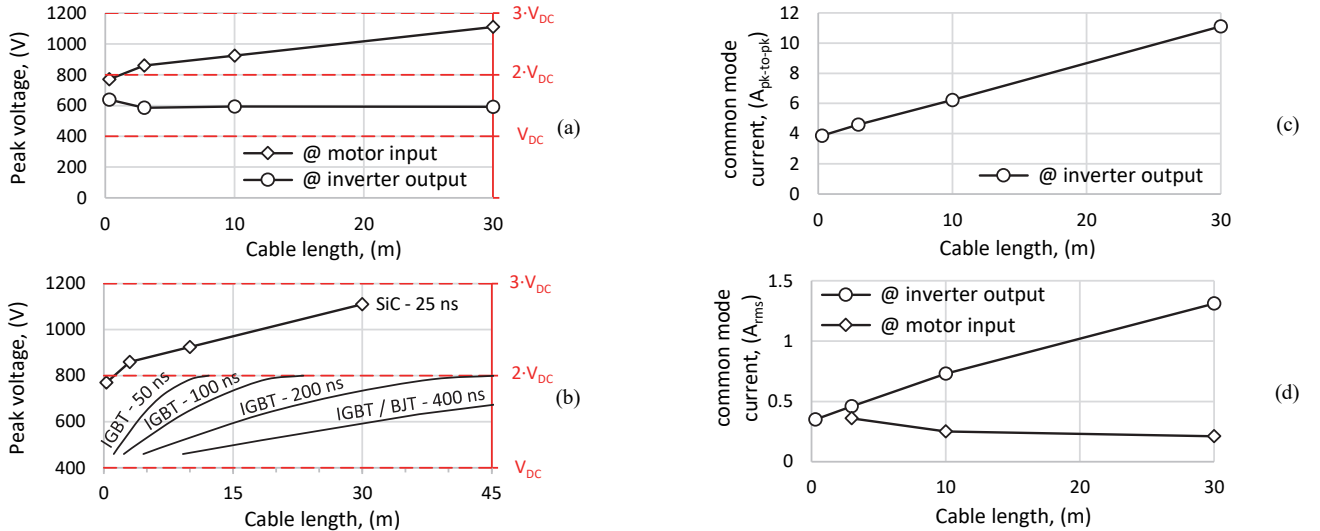


Fig. 9: The 'average' values of Table III versus the cable length: (a) the overvoltage at the cable ends, (b) the motor terminal overvoltage compared with other technologies and risetimes [11], (c) the peak-to-peak common mode current at the inverter output, and (d) the rms common mode current at the cable ends (markers for 0.3 m, 3 m, 10 m and 30 m cables).

In the presence of a severe common mode current flowing in the ground conductor, the Aron connection, shown in Fig. 8 on the left, cannot be used; the 4-wire connection, shown in Fig.8 on the right, must be used in its place. With the 4-wire connection, the total active power is computed by summing the readings of three equivalent wattmeters. It should be noted that the six voltage and current waveforms measured with this method allow to compute the instantaneous power flowing through the common mode path – see Section VII.C. Nonetheless, up to switching frequencies close to 25 kHz, it is experimentally verified that the active power $W_A + W_B$-measured with the Aron connection is nearly equal to the total active power $W_1 + W_2 + W_3$ absorbed by the motor, i.e. differences smaller than 1% have been observed. Therefore, at least up to these switching frequencies, the Aron connection is reasonably accurate in the measurement of active power.
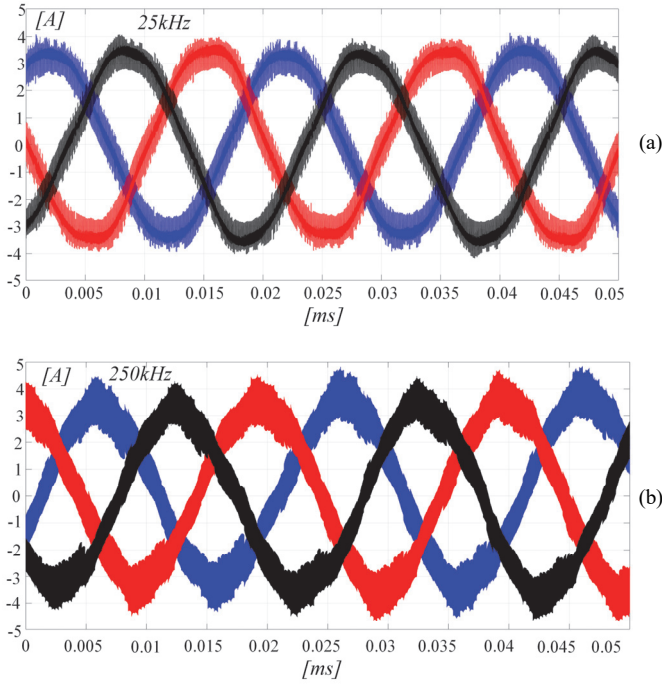
(a)

(b)

Fig. 10: Motor phase no load currents measured at rated fundamental voltage and 25 kHz and 250 kHz switching frequency.
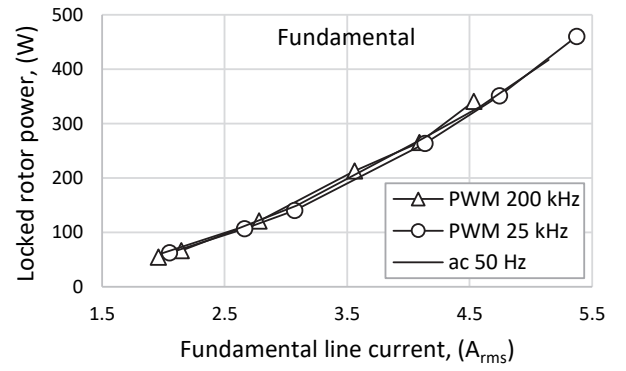


Fig. 11: Input power provided by the fundamental harmonic under locked-rotor conditions, for different switching frequencies, and standard ac test results.
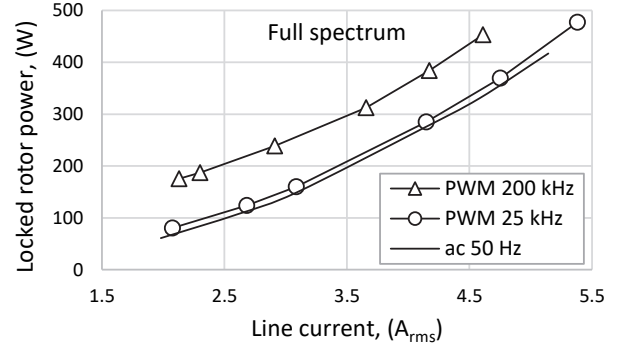


Fig. 12: Total (full spectrum) input power under locked-rotor conditions for different switching frequencies (standard ac test results is the comparison baseline).

## V. OVERVOLTAGE AND COMMON MODE CURRENT MEASUREMENTS

The experimental investigation is initially directed towards the study of overvoltages at the motor terminals and the common mode currents. As shown in Table III, the tests have been repeated for four cable lengths, from 30 cm to 30 m, and for six switching frequencies, from 25 kHz to 350 kHz.

During these measurements, the motor is running at the no load speed and at the maximum available voltage (i.e. the inverter is operated at unity amplitude modulation index). All the tests are conducted using deadtime and risetime equal to 0.15 µs and 25 ns, respectively.

The measurements for the 30 m cable setup are taken for switching frequencies only up to 100 kHz, to avoid residual current device tripping caused by excessive common mode currents. Table III shows that both the overvoltages and the common mode currents feature a limited variation with the switching frequency and a much more significant dependence with the cable length.

Figure 9a shows that the overvoltage at the motor terminals exceeds $2 \cdot V_{DC}$ (i.e. the theoretical value for the single pulse reflection) for cables shorter than 1 m. Additionally, significant voltage spikes are measured at the inverter output terminals, reaching values up to $1.5 \cdot V_{DC}$. Fig. 9b compares the measured overvoltages with those reported in the literature, clearly showing how the change from IGBTs to SiC MOSFETs and consequent reduction in device rise time introduces non-negligible wave reflections even for short cables, which aren't problematic for IGBTs.

The averaged peak-to-peak and RMS common mode current values measured at both the inverter and motor terminals are displayed in Fig. 9c and Fig. 9d, respectively (last column of Table III). The common mode current measured at the inverter terminals is characterized by 'impressive growth' with the cable length; the increase is almost linear with the cable length. Conversely, the common mode current measured at the motor terminals is substantially independent of the cable length, as shown in Fig. 9c.

## VI. LOCKED ROTOR AND NO-LOAD TESTS UNDER ULTRA-HIGH SWITCHING FREQUENCY PWM

Locked rotor and no-load tests are carried out by supplying the IM at different switching frequencies and amplitude modulation indices. All tests are executed by using the 3 m long cable. The oscilloscope probes are connected to the motor terminals in accordance with the connections reported in Fig. 8. Both connections are used for active power and common mode current measurements, to verify the agreement between the two.

The standard locked rotor and no-load tests aren't performed with the aim of identifying the fundamental frequency equivalent circuit parameters, but only to quantify the effects of the ultra-high switching frequency. However, these parameters can be computed by elaborating the fundamental quantities measured during the tests.
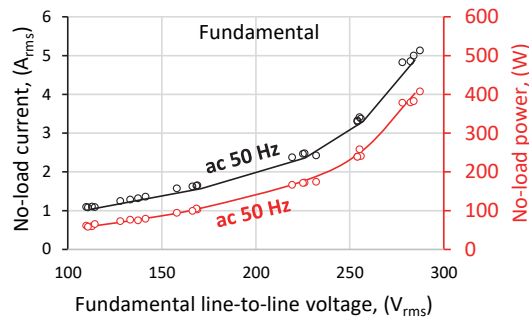
Fig. 13: No-load test results vs. the fundamental line-to-line voltage for different switching frequencies: fundamental no-load current (black), input power provided by the fundamental harmonic components (red).



Fig. 15: Total no-load power for different PWM switching frequencies and amplitude modulation index (standard ac test is the comparison baseline).
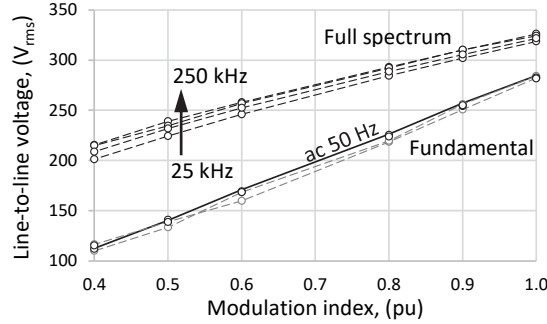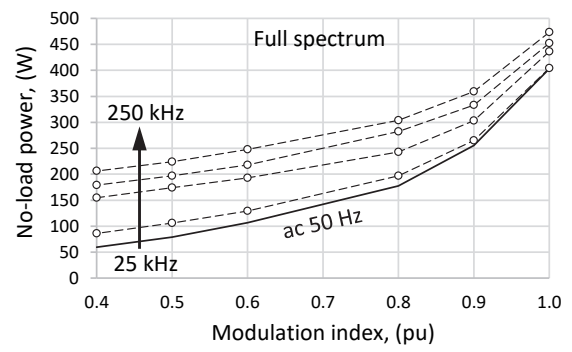


Fig. 14: Line-to-line voltage at no-load for different switching frequencies and amplitude modulation index (standard ac test is the comparison baseline).
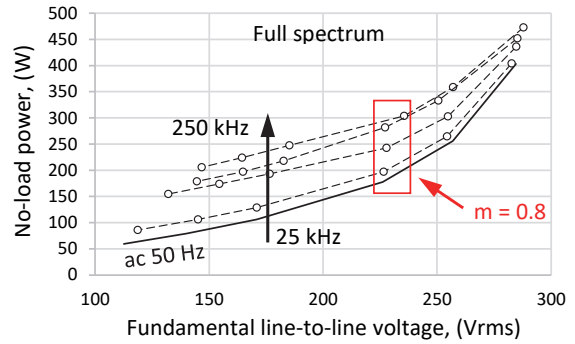


Fig. 16: Total no-load power for different PWM switching frequencies and fundamental line-to-line voltage (standard ac test is the comparison baseline).

In fact, also under ultra-high switching frequency, it is verified that the fundamental quantities are not dependent on the switching frequency; real-time Fourier analysis is a valuable tool to extract 50 Hz quantities from the instrument readings, [19]. Unfortunately, due to some limitations in the experimental setup standard temperature- and variable- load tests are not possible. For this reason, the no-load tests are extended beyond the rated fundamental voltage leading to line currents close to the rated value. Even if the rated current is reached in the tests, the magnetic flux in the machine is very different in locked rotor and no-load conditions since the amplitude modulation index is very different in the two cases. Finally, the tests are executed paying attention to avoid excessive overheating of the motor. Hence, the power supply is removed after each measurement.

The results shown in Fig. 10 are obtained by running the motor at no load and supplying it at the rated fundamental voltage, with a switching frequency equal to 25 kHz (Fig. 10a) and 250 kHz (Fig. 10b), respectively. The current signals displayed in Fig. 10 are filtered with a digital filter set to 750 kHz, for visualization purposes. The total harmonic current distortion $THD_i$ is computed for both operating conditions by considering the first 50 harmonics, leading to 3% and 3.8% respectively at 25 kHz and 250 kHz.

### A. Locked rotor tests

The locked rotor tests are performed for PWM switching frequencies equal to 25 kHz and 200 kHz, and the results are compared to those under *ac* mains supply. The fundamental and full spectrum powers are shown as function of the line current in Fig. 11 and Fig. 12, respectively.

During the locked rotor test, the amplitude modulation index is changed from 0.1 up to 0.25 to vary the fundamental supply voltage of the motor. For the two switching frequencies, the measured common mode currents are roughly independent of the amplitude modulation index and equal to 210 mA$_{rms}$ and 580 mA$_{rms}$, respectively.

Figure 11 shows the active power versus the fundamental line current; as expected, under PWM supply the switching frequency doesn't affect the fundamental components. However, the behaviour of the drive is quite different when the high frequency voltage harmonics are included in the computation of the active power, i.e. in full spectrum mode. In this last case, the results are reported in Fig. 12.

It is worth noting that the PWM introduces extra losses in the motor with respect to mains supply. An average increase of 40% of the absorbed power is measured at 200 kHz and is almost invariant with the line current (and line-to-line voltage). This finding motivates the authors to perform more in-depth analyses which are described in section VII, showing that the bulk of this increase is constituted by high frequency common mode losses.

### B. No-load tests

No-load tests at the PWM switching frequencies of 25, 100, 200, and 250 kHz are executed using the same *dc* bus voltage used in the previous tests (i.e. 400 V), and an amplitude modulation index varying from 0.4 to 1.0. The same cable length of the locked rotor tests is used. The results of these tests are summarized from Fig. 13 to Fig. 16.
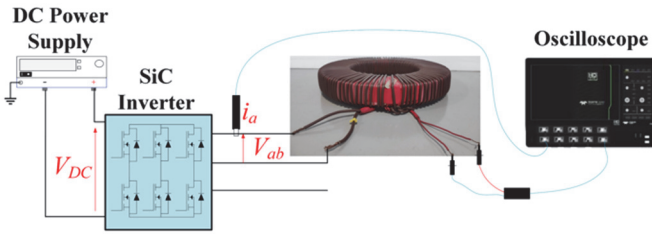
Fig. 17: Experimental setup for laminated steel iron loss measurements.

The circles in Fig. 13 depict the fundamental no-load components of the input current and the input power as function of the fundamental line-to-line voltage, for all the considered switching frequencies.

The results of the standard *ac* no-load test performed at 50 Hz (the black and red continuous trends in the figure) are added for comparison purposes. These results prove that the Fourier analysis can be considered as a suitable filtering technique to emulate standard no-load *ac* tests. In particular, the good agreement between the fundamental values and the ac 50 Hz results should be noted, both in linear and in heavy saturation conditions.

Figure 14 highlights the effects of the high frequency harmonic content on the RMS value of the line-to-line voltage at the motor terminals, both in terms of fundamental and full spectrum quantities. Even if the increase of the rms full spectrum values with respect to fundamental counterparts is trivial, their dependence with the switching frequency is not. It is found that the rms full spectrum voltage at the motor terminals increases monotonically with the switching frequency and with the reduction of the amplitude modulation index.

This phenomenon is due to the different behaviour that the 3 m cable exhibits at the different switching frequencies. On the other hand, the fundamental component of the voltage doesn't depend on the switching frequency. This is experimentally verified for the 25 kHz and 100 kHz cases (where the black circles are perfectly overlapped with the *ac* 50 Hz shown in Fig. 14), while for the 200 kHz and 250 kHz values (the gray dashed trends in the same figure) a slightly wider spread in the measurements is observed.

Figure 15 and Fig. 16 show the increase of the no-load power absorbed by the IM from two different viewpoints: the former presents the results as a function of the amplitude modulation index; the latter shows the same values versus the fundamental line-to-line voltage measured at the motor terminals. Figure 15 represents what happens inside the IM and it can be derived only if the modulation index is known, while Fig. 16 can be easily obtained by the drive user by measuring the power directly at the motor terminals. Additionally, it is interesting to observe the regularity of the trends shown in Fig. 15 with respect to the ones reported in Fig. 16, which are 'noisier' due to the presence of 3 m long cable. However, both figures show that for a fixed switching frequency, the extra losses due to the PWM supply tend to increase at low modulation indexes. This is mainly due to high frequency common mode losses, as explained in section VII. At the fundamental rated voltage (obtained with an amplitude modulation index m = 0.8 for all the switching frequencies) the increase of the no-load losses is small up to 25 kHz.

Vice versa, with respect to the mains supply, significant increases in the active power have been observed when the machine is operated at switching frequencies above 100 kHz (e.g. + 70 % @ m = 0.8 and $f_{sw}$ = 250 kHz).

## VII. DISCUSSION

Figure 12 and Fig. 16 demonstrate that the input power variations unquestionably depend on the switching frequency, both in locked rotor and no-load conditions. However, a better interpretation of the dissipative phenomena under sub-MHz PWM is necessary to split the total losses into their basic contributions. For this purpose, further experimental analyses were undertaken, and the results are briefly summarized in the following paragraphs.

### A. Iron losses in a toroidal core

Firstly, it should be considered that the iron losses computed by elaborating the standard no-load tests must be considered as '*conventional*' iron losses, because they account also for other contributions having different nature. For example, already under sinusoidal supply there are Joule losses in the rotor bar due to the spatial magneto-motive force harmonics rotating at speeds other than synchronism, [20]. Hence, sub-MHz PWM effects on the '*pure*' iron losses are experimentally investigated by testing a toroidal sample made with the same laminations (M800-50A) used for the motor magnetic cores. As shown in Fig. 17, the toroid is equipped with a primary winding to magnetize the magnetic core at the desired magnetic field strength and with a secondary winding to measure the induced voltage; flux density and iron losses in the magnetic core are obtained by elaborating the measured primary current and secondary voltage, [21].

The primary voltage coincides with the line-to-line voltage of the same inverter used during the motor tests. Since the inverter legs are modulated according to a PWM with unipolar voltage switching, extra-iron losses due to minor hysteresis loops are not present, [15], [16]. In fact, a necessary and sufficient condition to avoid minor hysteresis loops is that the fundamental voltage waveform should have the same sign of the supply voltage waveform, on an instantaneous basis. Additionally, the measurements highlight that the overall magnetization condition doesn't depend on the switching frequency – see Fig. 18.
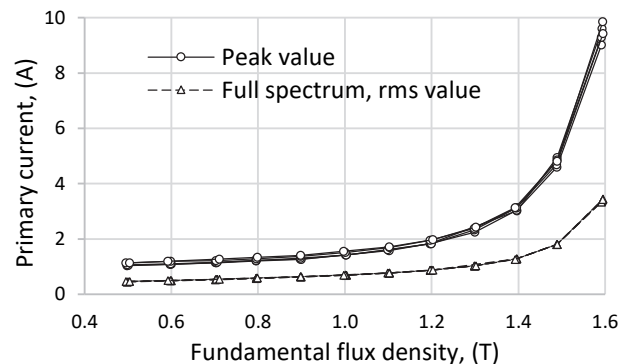


Fig. 18: Primary winding current in the toroidal core as function of the fundamental flux density for all the considered PWM switching frequencies.
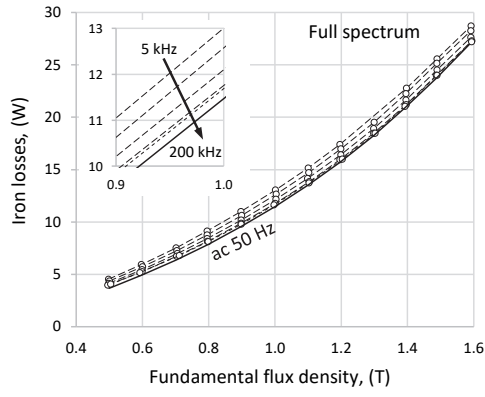
Fig. 19: Core losses vs. the fundamental flux density for switching frequencies of 5, 10, 25, 100 and 200 kHz (dashed curves) and *ac* 50 Hz (continuous line).
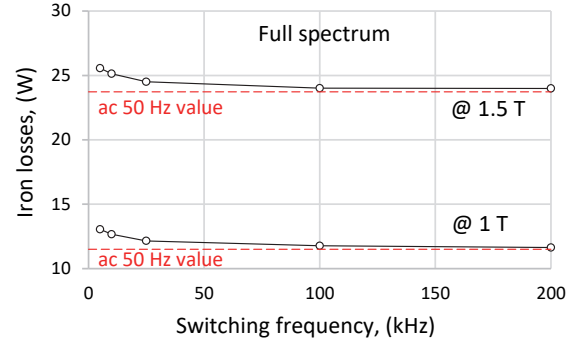


Fig. 20: Iron losses in the toroidal core as function PWM switching frequency for the fundamental flux density equal to 1 T and 1.5 T.

TABLE IV
COMMON MODE VOLTAGE AND CURRENT WAVEFORMS AND HARMONIC CONTENT FOR DIFFERENT MOTOR DRIVE OPERATING CONDITIONS

Fig. 21: Rms common mode voltage measured during the locked-rotor and no-load tests at 25 kHz and 200 kHz, where the ellipses highlight the four operating conditions of Table IV.



Fig. 22: Rms common mode current measured during the locked-rotor and no-load tests at 25 kHz and 200 kHz, where the ellipses highlight the four operating conditions of Table IV.

Results reported in Fig. 19 and Fig. 20 confirm that the iron losses monotonically decrease with the switching frequency, [16]. Therefore, the '*pur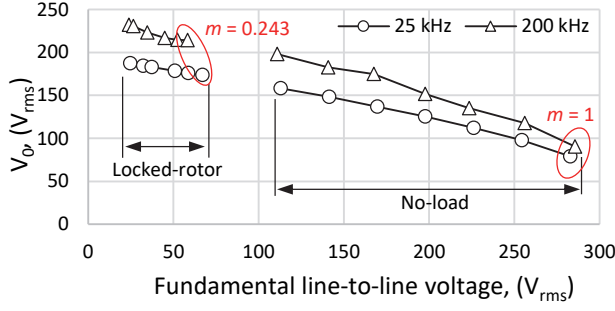e*' iron losses in the magnetic motor cores should also drop slightly at high switching frequency; it is therefore necessary to find other possible explanations for the non-negligible loss growths observed in the no-load and locked rotor operations.

*B. Measurement of common mode voltages and currents*

The 4-wire connection shown on the right of Fig. 8 allows to measure common mode voltage $v_0(t)$ and common mode current $i_0(t)$ at the motor terminals. As well known, these quantities can be determined according to [22]:

$$\begin{cases} i_0(t) = [i_R(t) + i_S(t) + i_T(t)]/3 \\ v_0(t) = [v_{R\_GND}(t) + v_{S\_GND}(t) + v_{T\_GND}(t)]/3 \end{cases} \quad (2)$$

The measurements of the above common mode quantities are carried out through a detailed experimental campaign of no-load and locked rotor tests performed with the inverter-3 m cable system PWM operated at 25 kHz and 200 kHz.

Considering the unavoidable fluctuations in power measurements under PWM supply, the tests aree considered reliable when the fundamental quantities at the motor terminals are in close agreement with those measured under sinusoidal supply. Both common mode voltage and current include only high frequency harmonics and, in general, they are quite challenging to measure. This is particularly true for the common mode current due to its small amplitude, as proven by the waveforms' harmonic spectra shown in Table IV.

Looking at the figures reported in this table, the common mode current harmonics are obviously more impacting for the 200 kHz PWM case. Anyhow, still looking at Table IV, it is interesting to observe how the common mode waveforms and spectra change with respect to locked rotor and no-load operations. In fact, as for the fundamental components, also the high frequency harmonics introduced by PWM see a different impedance at the motor terminal at standstill and at synchronous speed. Figure 21 and Fig. 22 show the total *rms* value of the common mode voltage and current as function of the fundamental line-to-line voltage applied to the motor terminal. The measurements prove that, also in presence of the 3 m cable, the correlation between the motor fundamental voltage and the modulation index is linear; these trends can be equivalently interpreted as function of the modulation index.
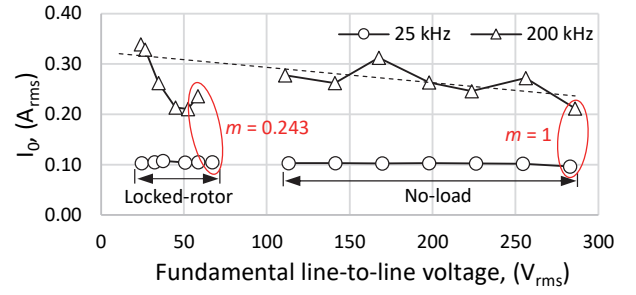
Moreover, Fig. 21 and Fig. 22 graphically prove whether the harmonics of the common mode quantities at 25 kHz and 200 kHz are or not the dominating harmonics in the corresponding total *rms* values. In particular, the *rms* value of the common mode voltage is comparable with the amplitude of switching harmonic of $v_0(t)$, but this isn't the case for the common mode current.

Fig. 21 shows that the trends of the common mode *rms* voltage at 25 kHz and 200 kHz are similar, but slightly dependent on the switching frequency, probably for a voltage divider effect of the output inverter voltage on the cable-motor series. It is important to keep in mind that the motor can be considered as a linear R-L load during the locked-rotor test and as a saturable inductance in no-load operation. On the other hand, the evident dependence of these trends with the amplitude modulation index requires further investigations on the voltage and current spectra at the inverter output and a detailed modelling of the cable-motor system, which is not within the scope of this study.

With regards to the common mode current (see Fig. 22), the *rms* values are substantially constant with the fundamental line-to-line voltage, at least at 25 kHz switching frequency. The increase of the *rms* values from 25 kHz and 200 kHz is an obvious and direct consequence of the common mode current being due to capacitive effects. The trend at 200 kHz is characterized by a large spread in the results, proving the challenges to performs such a type of measures. However, the regression line of the common mode current values measured during the no-load test at 200 kHz shows that also in this case the dependence by the modulation index is marginal.

Finally, in locked rotor conditions at 200 kHz (the trend in the upper left corner of Fig. 22), it is the authors' opinion that the last triangular markers are far from the regression line not because of inconsistence or errors in the measurements, but due to possible resonances in the cable-motor system.

*C. Common mode active power and harmomic losses*

When $v_0(t)$ and $i_0(t)$ are known, the active power $P_0$ associated to the common mode sequence can be computed according to (3).

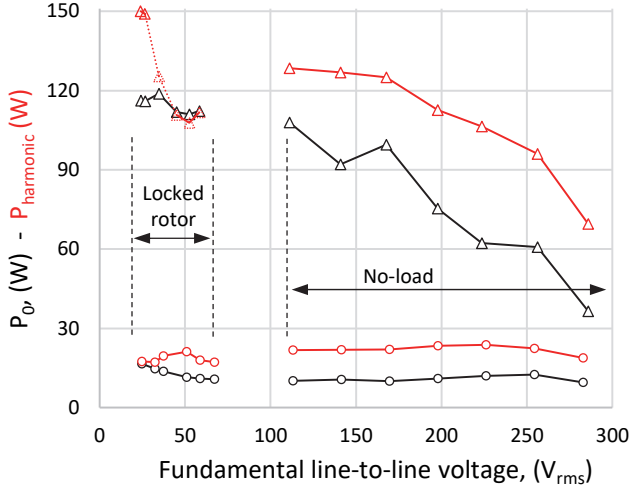$$P_0 = \frac{1}{T}\int_0^T 3 \cdot v_0(t)i_0(t)dt \quad (3)$$

Fig. 23: Common mode losses $P_0$ and harmonic losses $P_{harmonic}$ vs. the fundamental line-to-line voltage at different switching frequency (circles = 25 kHz, triangles = 200 kHz).

The results are the black trends reported in Fig. 23. The measurements of $P_0$ can be considered even more challenging because also very short time shift between the signals affects the results leading, also in no-load conditions, to a larger spread of the results at high switching frequency. However, clear trends can be appreciated in the figure and, consequently, considered as a flag of the measurement reliability.

Figure 23 also shows the so-called '*harmonic losses*' $P_{harmonic}$, defined as the difference between the full-spectrum input power ($W_1 + W_2 + W_3$, see Fig. 8) and the corresponding fundamental active power at the motor inputs. This means that $P_{harmonic}$ describes all the high frequency harmonic effects introduced in the motor by the PWM with respect to the sinusoidal supply, [19]. Then, the distance from the black and red trends graphically depicts all the PWM harmonic losses different from those associated to the common mode (i.e. additional iron losses in the magnetic materials excited by the leakage fluxes, eddy current losses in conductive materials, etc.).

The measurements shown in Fig. 23 are extremely important because they prove that at high switching frequency the largest part of the harmonic losses is associated to the common mode, both in locked rotor and in no-load conditions. The roughly 100 W increase in common mode losses from 25 kHz to 200 kHz under locked rotor matches the similar increase shown in Fig. 12. Additionally, the common mode losses in no load conditions tend to increase as the amplitude modulation index decreases, confirming that the trends shown in Fig. 15 and Fig. 16 are dominated by this loss contribution. It is worth mentioning that the international standards for efficiency labelling for inverter-fed induction motors assume that the additional harmonic losses are constant when changing from no-load to load operations. Therefore, under sub-MHz PWM supply, efforts must be done to limit the parasitic effects of common mode paths in the cable-motor system, possibly by introducing a special design of the electrical machine and/or suitable control techniques of the WBG-based inverter.

## VIII. CONCLUSION

The above results clearly show the importance of testing electric motors supplied by WBG-based inverters with switching frequencies up to 350 kHz. The performed test campaigns represent a starting point to obtain a clearer picture of the effects of ultra-high switching frequencies on induction motors. Key conclusions that can be drawn by the experimental observations presented in the paper are:

- Overvoltages and common mode currents reach levels that warrant highly integrated WBG motor-drives, without any cable between the inverter and the motor;

- With respect to active power measurement methods, the Aron connection should be used with great caution since it does not allow to correctly measure the active power due to the high frequency common mode. It has been experimentally proven that for switching frequencies above 25 kHz a four-wire connection must be adopted, especially when performing comparative no-load tests between mains and inverter supplies, in accordance with international standards for IM efficiency determination under PWM supply (e.g. the IEC 60034-2-3);

- Above switching frequencies of 25 kHz, it has been experimentally determined that stator and rotor Joule losses slightly increase with the switching frequency due to an equally small increase of the rms phase current, while the classical core iron losses significantly decrease (in particular, above 100 kHz);

- Harmonic losses increase with switching frequency because of the active power dissipated in the common mode paths and of additional losses occurring in the magnetic and electrical circuits of the machine. This study reveals that the common mode losses constitute the bulk of the total harmonic losses when the switching frequency exceeds 50 kHz, making a clear separation of the additional losses into their constitutive components less stringent. It is the authors' opinion that this segregation is methodologically unfeasible without corroborating the experimental observations with finite element analyses (FEA). However, the implementation of suitable FEA models which take high-switching frequency modulation effects into account is still an open research field;

- Based on the above, it is concluded that conventional WBG-based PWM inverters shouldn't be used to supply standard production induction motors, when they are operating at their highest switching frequencies, at the fastest device rise times and in the presence of cables, even if short. In order to completely generalize this conclusion, the authors are working on a wider testing campaign involving different sizes of both mains- and PWM inverter-designed induction machines, with a focus on highly-integrated motor drives.

## REFERENCES

[1]. A. K. Morya, *et al.*, "Wide bandgap devices in AC electric drives: opportunities and challenges," *IEEE Trans. Transport. Electrific.*, vol. 5, no. 1, pp. 3-20, Jan. 2019.

[2]. B. J. Baliga, *Gallium Nitride and Silicon Carbide Power Devices*, Singapore: World Scientific Publishing, 2017.

[3]. "Power Sic 2019: Materials, Devices, and Applications report", Yole Developpement, 2019, available on line at https://www.slideshare.net/Yole_Developpement.

[4]. "Power GaN 2017: Epitaxy, Devices, Applications, and Technology Trends 2017 report", Yole Developpement, 2017, available on line at https://www.slideshare.net/Yole_Developpement.

[5]. M. Lapedus, "Power semi wars begin: They won't replace silicon, but GaN and SiC are becoming much more attractive as prices drop", Manufacturing, Packaging & Materials, Oct. 2019, on line.

[6]. Z. Liu, and G. L. Skibinski, "Method to reduce overvoltage on AC motor insulation from inverters with ultra-long cable," in Proc. *IEEE IEMDC*, Miami, FL, 2017, pp. 1-8.

[7]. H. Xiong, J. Zhang, and A. Von Jouanne, "Control of variable frequency drive PWM to mitigate motor overvoltage due to double pulsing in reflected wave phenomenon," in *Proc. IEEE ECCE*, Portland, OR, USA, 2018, pp. 6563-6570.

[8]. R. Leuzzi, V. G. Monopoli, L. Rovere, F. Cupertino, and P. Zanchetta, "Analysis and detection of electrical aging effects on high-speed motor insulation," *IEEE Trans. Ind. Appl.*, vol.55, no.6, pp. 6018-6025, Nov./Dec. 2019.

[9]. C. Abadie, T. Billard, and T. Lebey, "Partial discharges in motor fed by inverter: from detection to winding configuration," *IEEE Trans. Ind. Appl.*, vol. 55, no. 2, pp. 1332-1341, 2019.

[10]. R. Ruffo, P. Guglielmi, and E. Armando, "Inverter side RL filter precise design for motor overvoltage mitigation in SiC-based drives," *IEEE Trans. Ind. Elect.*, vol. 67, no. 2, pp. 863-873, Feb. 2020.

[11]. R.J. Kerkman, D. Leggate, and G.L. Skibinski, "Interaction of drive modulation and cable parameters on AC motor transients," *IEEE Trans. on Ind. Appl.*, vol. 33, no. 3, pp. 722-731, May/Jun. 1997.

[12]. E. Persson, "Transient effects in application of PWM inverters to induction motors," *IEEE Trans. on Ind. Appl.*, vol. 28, no.2, pp. 1095-1101, Sep./Oct. 1992.

[13]. A. F. Moreira, T. A. Lipo, G. Venkataramanan, and S. Bernet, "High-frequency modeling for cable and induction motor over-voltage studies in long cable drives," *IEEE Trans. Ind. Appl.*, vol. 38, no. 5, pp. 1297–1306, Sep./Oct. 2002.

[14]. H. Dai, R.A. Torres, W. Lee, T. M. Jahns, and B. Sarlioglu, "High-frequency evaluation of two-level voltage-source and current-source inverters with different output cables," in *Proc. IEEE ECCE*, Detroit, MI, USA, 2020, pp. 2403-2410.

[15]. I. Sirotić, M. Kovačić and S. Stipetić, "Methodology and measurement setup for determining PWM contribution to iron loss in laminated ferromagnetic materials," *IEEE Trans. Ind. Appl.*, vol. 57, no. 5, pp. 4796-4804, Sep./Oct. 2021.

[16]. L. Chang, W. Lee, T. M. Jahns, and K. Rahman, "Investigation and prediction of high-frequency iron loss in lamination steels driven by voltage-source inverters using wide-bandgap switches," *IEEE Trans. on Ind. Appl.*, vol. 56, no.2, pp. 3607-3618, Jul./Aug. 2021.

[17]. G. Scelba, *et al.*, "On the effects of ultra-high switching frequency on PWM-inverter-fed induction motors," in *Proc. IEEE ECCE*, Detroit, MI, USA, 2020, pp. 3823 - 3830.

[18]. M. Cacciato, A. Consoli, G. Scarcella, and A. Testa, "Reduction of common-mode currents in PWM inverter motor drives," *IEEE Trans. Ind. Appl.*, vol. 35, no. 2, pp. 469-476, Mar./Apr. 1999.

[19]. E. B. Agamloh, A. Cavagnino, and S. Vaschetto, "Standard efficiency determination of induction motors with a PWM inverter source," IEEE Trans. Ind. Appl., vol. 55, no. 1, pp. 398-406, Jan./Feb. 2019.

[20]. A. Cavagnino, *et al.*, "Striving for the Highest Efficiency Class with Minimal Impact for Induction Motor Manufacturers," *IEEE Trans. Ind. Appl.*, vol. 56, no. 1, pp. 194-204, Jan.-Feb. 2020.

[21]. IEC 60404-6, *Magnetic Materials – Part 6: Methods of measurement of the magnetic properties of magnetically soft metallic and powder materials at frequencies in the range 20Hz to 100kHz by the use of ring specimens*, International Electrotechnical Commission Std. Second edition, May 2018.

[22]. E. Clarke, "Circuit Analysis of A-C Power Systems, Volume 1: Symmetrical and Related Components," New York, John Wiley & Sons Inc, 1948, Vol. I.

**Giacomo Scelba** (S'04, M'07, SM'17) was born in Caltagirone, Italy. He received the M.S. and Ph.D. degrees in electrical engineering from the University of Catania, Catania, Italy, in 2002 and 2006, respectively. He is currently an Associate Professor with the Department of Electrical Electronic and Computer Engineering (DIEEI), University of Catania. He is a co-PI of a collaborative research agreement between the DIEEI and the Department of Astronautical, Electrical and Energy Engineering, Sapienza-University of Rome, for research in the field of wide-bandgap-semiconductor-based drives. His current research interests include sensorless control strategies, ac drive control technologies, fault-tolerant motor drives, modeling and control of power converters and advanced technologies for power electronics applications. Prof. Scelba is a Member of the IEEE Industry Applications, the IEEE Industrial Electronics, and the IEEE Power Electronics Societies. He is a Member of the IEEE IAS Industrial Drives Committee, the IAS Electric Machines Committee, the IAS Industrial Power Converters Committee, the PELS Technical Committee on Electrical Machines, Drives and Automation and the IES Electrical Machines Committee. He was a recipient of the 2014 First Prize Paper Award and the 2016 Third Prize Paper Award, both from the IAS Industrial Drives Committee, and the 2018 Third Prize Paper Award from the IES Electrical Machine Technical Committee. He is currently serving as an Associate Editor for the IEEE TRANSACTIONS ON INDUSTRY APPLICATIONS.

**Daniele Cremente** received the B.S. degree in industrial engineering and M.S. degree in electrical engineering from the University of Catania, Catania, Italy, in 2017 and 2021, respectively. He is currently a fellow researcher at the Department of Electrical Electronic and Computer Engineering (DIEEI), University of Catania. His research interests include electrical drives control and digital signal processing techniques.

**Giulio De Donato** (S'05, M'08, SM'17) was born in Cork, Ireland. He received the M.S. and Ph.D. degrees in electrical engineering from Sapienza-University of Rome, Italy, in 2003 and 2007, respectively.
He is an Associate Professor with the Department of Astronautical, Electrical and Energy Engineering (DIAEE), Sapienza-University of Rome. He is Co-PI of a collaborative research agreement between the DIAEE and the Department of Electrical, Electronic Engineering, and Computer Science, University of Catania, for research in the field of wide-bandgap semiconductor-based drives. His current research interests include digital control of brushless drives, and analysis and design of permanent magnet machines and of wide-bandgap-semiconductor-based power converters. Prof. De Donato is a Member of the IEEE Industry Applications, the IEEE Power Electronics and the IEEE Industrial Electronics Societies. He is a Member of the IEEE IAS

Industrial Drives Committee, the IAS Electric Machines Committee, the PELS Technical Committee on Electrical Machines, Drives and Automation and the IES Electrical Machines Committee. Currently, he is the Secretary of the IAS Electric Machines Committee. He was a recipient of the 2014 First Prize Paper Award and of the 2016 Third Prize Paper Award, both from the IAS Industrial Drives Committee. He was acknowledged as an Outstanding Reviewer for the IEEE TRANSACTIONS ON POWER ELECTRONICS in 2020. He is serving as an Associate Editor for the IEEE TRANSACTIONS ON INDUSTRY APPLICATIONS and for the IEEE TRANSACTIONS ON POWER ELECTRONICS.

**Silvio Vaschetto** (S'10–M'13–SM'19) received the M.Sc. and Ph.D. degrees in electrical engineering from the Politecnico di Torino, Italy, in 2007 and 2011, respectively. He then joined ABB IEC LV Motors Technology Center, Vittuone, Italy as R&D engineer. From 2012 to 2014 he was with Magna Electronics Italy, as Electromagnetic Simulation and Motor Design Engineer. He is currently an Associate Professor at the Energy Department "G. Ferraris", Politecnico di Torino. His research interests include electromagnetic design, thermal design, and energetic behavior of electrical machines for high-performance applications. Prof. Vaschetto is Associate Editor for IEEE TRANSACTIONS ON INDUSTRY APPLICATIONS and for *IET Electric Power Applications*.

**Emmanuel B. Agamloh** (S'02–M'05–SM'09) received the B.Sc. and M.Sc. degrees in electrical engineering from St. Petersburg State Technical University, St. Petersburg, Russia, in 1992 and 1994, respectively, and the Ph.D. degree in electrical and computer engineering from Oregon State University, Corvallis, OR, USA, in 2005. He is an Associate Professor with the Department of Electrical and Computer Engineering, Baylor University, Waco, TX, USA. His research interests include electric machine design, analysis, and testing and renewable energy with application areas, such as industrial, aerospace, transportation, and oil and gas. Dr. Agamloh received two IEEE First Prize Paper Awards for his research. His extensive industry experience includes a 14-year role as Technical Director of the Motors and Drives Laboratory at Advanced Energy Corporation in Raleigh, NC, USA. He was a Technical Paper Review Chair of the IEEE TRANSACTIONS ON INDUSTRY APPLICATIONS and a past Chair of the IEEE-IAS Electric Machines Committee. He is the General Chair of the 2022 IEEE Energy Conversion Congress and Exposition (ECCE) to be held in Detroit, Michigan.

**Andrea Cavagnino** (M'04–SM'10–F'20) was born in Asti, Italy, in 1970. He received his M.Sc. and Ph.D. degrees in electrical engineering from the Politecnico di Torino, Italy, in 1995 and 2000, respectively. He is a professor at the Politecnico di Torino. He has authored or co-authored more than 250 papers, receiving four Best Paper Awards. His research interests include electromagnetic design, thermal design, and energetic behaviour of electrical machines. He usually cooperates with factories for a direct technological transfer and he has been involved in several public and private research projects. Prof. Cavagnino is an Associate Editor of the IEEE TRANSACTIONS ON ENERGY CONVERSION (TEC), a Past Chair of the Electrical Machines Technical Committee of the IEEE Industrial Electronics Society, a past Associate Editor of the IEEE TRANSACTIONS ON INDUSTRIAL ELECTRONICS (TIE), and the IEEE TRANSACTIONS ON INDUSTRY APPLICATIONS. He was also a Guest Editor of six Special Sections for IEEE-TIE and co-Editor in Chief of a Special Issue for IEEE-TEC. Prof. Cavagnino was a technical program chair of the IEEE-IEMDC 2015 and IEEE-ECCE 2022 conferences. He is a reviewer for several IEEE TRANSACTIONS and other international journals and conferences.